A study of the morphology and effective density of externally mixed black carbon aerosols in ambient air using a size-resolved single-particle soot photometer (SP2)

Yunfei Wu[1*], Yunjie Xia[1, 2], Rujin Huang[3], Zhaoze Deng[4], Ping Tian[5], Xiangao Xia[4], Renjian Zhang[1*]

1 Key Laboratory of Regional Climate-Environment for Temperate East Asia (RCE-TEA), Institute of Atmospheric Physics, Chinese Academy of Sciences, Beijing 100029, China

2 University of Chinese Academy of Sciences, Beijing, 100049, China

3 Key Laboratory of Aerosol Chemistry and Physics, State Key Laboratory of Loess and Quaternary Geology, Institute of Earth and Environment, Chinese Academy of Sciences, Xi'an 710061, China

4 Key Laboratory of Middle Atmosphere and Global Environment Observation (LAGEO), Institute of Atmospheric Physics, Chinese Academy of Sciences, Beijing 100029, China

5 Beijing Weather Modification Office, Beijing 100089, China

Correspondence to: Yunfei Wu (wuyf@mail.iap.ac.cn) and Renjian Zhang (zrj@mail.iap.ac.cn)

Abstract

The morphology and effective density of externally mixed black carbon (*ext*BC) aerosols, important factors affecting the radiative forcing of black carbon, were studied by using a tandem technique coupling a differential mobility analyzer (DMA) with a single-particle soot photometer (SP2). The study extended the mass-mobility relationship to large *ext*BC particles with a mobility diameter (d_{mob}) larger than 350 nm, a size range was seldom included in previous tandem measurements of BC aggregates in the atmosphere. The experiment was conduct at an urban site in Beijing during a 19-day winter period from 23 January to 10 February 2018. Ambient dry particles were selected by the DMA, and the size-resolved *ext*BC particles were distinguished from particles with a thick coating (internally mixed) according to the time delay between the incandescence signal peak and the scattering peak detected by the SP2.The masses of the *ext*BC particles were then quantified. The time differences between the DMA

size selection and the SP2 measurement were processed previously. The normalized number size distributions were investigated at the prescribed d_{mob} sizes in the range of 140–750 nm to provide the typical mass of extBC at each d_{mob}. On this basis, the mass-mobility relationship of the ambient extBC was established, inferring a mass-mobility scaling exponent (D_{fm}) (an important quantity for characterizing the morphology of fractal-like BC aggregates) with a value of 2.34±0.03 in the mobility range investigated in this study. This value is comparable with those of diesel exhaust particles, implying a predominant contribution of vehicle emissions to the ambient extBC in urban Beijing. Compared to the clean period, a higher D_{fm} value was observed in the polluted episode, indicating a more compact BC aggregate structure than that in the clean period. The effective densities (ρ_{eff}) of the extBC in the same d_{mob} range were also derived, with values gradually decreasing from 0.46 g cm^{-3} at 140 nm mobility to 0.14 g cm^{-3} at 750 nm mobility. The ρ_{eff} values were slightly lower than those measured using the DMA-aerosol particle mass analyzer (APM) system. The difference in ρ_{eff} values was likely due to the lower BC masses determined by the SP2 compared to those measured by the APM at the same mobility, since the SP2 measured the refractory BC (rBC) mass instead of the total mass of the BC aggregate, which consists of both rBC and a possible fraction of nonrefractory components measured by the APM. Higher ρ_{eff} values were observed in the 280–350 nm d_{mob} range, and were much closer to the values for soot aggregates reported in the literature. The higher ρ_{eff} values might be related to the more compact structure of BC aggregates in this range, resulting from the reconstruction effect by volatile and/or semivolatile components in the atmosphere. The reconstruction effect might also result in a hiatus in the increased dynamic shape factor in the range of 200–350 nm which generally increased from 2.16 to 2.93 in the 140–750 nm d_{mob} range.

1 Introduction

Black carbon (BC), a byproduct of incomplete combustion, is the main light-absorbing component in atmospheric aerosols. BC can lead to positive radiative forcing only second to CO_2 and thus warming of the earth's atmosphere (IPCC, 2013). However, there remains a large amount of uncertainty regarding the radiative forcing induced by

BC due to its complexity and variability in morphology, mixing state and hygroscopicity. Freshly emitted BC particles usually exhibit as fractal-like aggregates made up of a number of primary carbon spherules (Park et al., 2004; Sorensen, 2011), which are generally hydrophobic. The condensation of organic and/or inorganic components leads to the collapse of the fractal-like aggregates and, in turn, a compact structure of BC particles (Slowik et al., 2007; Zhang et al., 2008). Changes in the morphology of BC particles affect their optical properties. Encasement by organic and/or inorganic coatings also increases the absorption of BC particles through the lensing effect (Shiraiwa et al., 2010; Peng et al., 2016). In addition, water-soluble coatings increase the hydrophilic ability of the BC particles (Zhang et al., 2008; McMeeking et al., 2011), indirectly affecting the radiative forcing by affecting the cloud processes.

Laboratory studies indicate that freshly emitted BC particles can be thickly coated within a few hours in the atmosphere (Pagels et al., 2009; Peng et al., 2016). Thus, many studies have focused on the optical properties and radiative forcing of thickly-coated BC particles (Jacobson, 2001; Khalizov et al., 2009; Liu et al., 2017). However, *in situ* measurements have shown that a great number of uncoated and/or thinly-coated BC particles exist in the ambient atmosphere, with a fraction even higher than that of the aged BC particles (Schwarz et al., 2008). In general, thickly-coated BC particles account for <50% of the BC-containing particles in urban areas based on single-particle soot photometer (SP2) measurements (Huang et al., 2012; Wang et al., 2014; Wu et al., 2016). The existence of a large fraction of uncoated and/or thinly-coated BC particles is likely due to continuous emission from combustion processes such as vehicle exhaust (Wang et al., 2017). Therefore, studies on the radiative forcing of BC particles without thick coatings are also essential, especially in urban areas. First, the morphologies and sizes of these quasi-bare BC particles, which are the essential quantities for calculating the optical properties of BC particles in numerical models, should be investigated (Scarnato et al., 2013; Bi et al., 2013).

The morphology of fractal-like BC aggregates is generally characterized by a quantity called 'fractal dimension' (D_f), which has been well documented in the review literature

89   (Sorensen, 2011). The ideal diffusion-limited cluster aggregation (DLCA), to which the

90   BC aggregates belong, has a D_f value of 1.78 ± 0.1. Recent studies have also reported

91   a similar D_f value of ~1.82 for bare-like soot particles by using transmission electron

92   microscopy (TEM) analysis of aerosol samples collected in four different environments

93   (Wang et al., 2017). A significant increase in the D_f was observed when the soot

94   particles were partly coated or embedded. In the past two decades, the morphologies of

95   the BC aggregates were also widely studied by using tandem mobility techniques (Park

96   et al., 2008). Measurements obtained by using an impactor (e.g., the electrical low-

97   pressure impactor (ELPI)) or a particle mass analyzer (e.g., the aerosol particle mass

98   analyzer (APM), the centrifugal particle mass analyzer (CPMA)) connected in tandem

99   with a differential mobility analyzer (DMA) revealed the relationship between particle

100   mass and mobility (Park et al., 2003; Maricq and Xu, 2004; Olfert et al., 2007; Rissler

101   et al., 2014; Sorensen, 2011; and associated references therein). The derived mass-

102   mobility scaling exponents (D_{fm}) which were also called 'fractal dimensions' in some

103   of these references varied in a wide range of 2.2–2.8 for diesel exhaust particles. These

104   values were inherently higher than the virtual D_f due to the improper interpretation of

105   mobility measurements, which was demonstrated in detail in Sorensen (2011). The D_f

106   of diesel particles obtained using TEM is ~1.75, corresponding to a large D_{fm} value of

107   ~2.35 obtained from the mass-mobility relationship (Park et al., 2004). The mobility

108   size-dependent effective densities (ρ_{eff}) of BC aggregates were also determined from

109   the DMA-ELPI or DMA-APM (or CPMA) measurements which were difficult to

110   characterize using the TEM techniques.

111   The previous tandem measurements generally provided the mass-mobility relationship

112   of particles with a mobility diameter (d_{mob}) not exceeding 350 nm due to the system

113   detect limit (Park et al., 2003; Maricq and Xu, 2004; Olfert et al., 2007; Rissler et al.,

114   2014). A condensation particle counter (CPC) is connected next to the DMA-APM

115   system to measure the number concentrations of mobility size-selected particles at

116   various APM voltages. The voltage is proportional to the particle mass, and the voltage

117   resulting in the maximum concentration is considered the typical voltage, in turn, of the

118   mass of particles with a prescribed mobility size. Because the larger particles (e.g.,

119   d_{mob}>350 nm) are less abundant in the atmosphere than the smaller particles, larger

120   uncertainties exist in the DMA-APM-CPC measurements for these larger particles

121   (Geller et al., 2006). The applicability of the mass-mobility relationship established on

122   the basis of tandem measurements of smaller mobility diameters (e.g., d_{mob}<350 nm) to

123   larger particles (e.g., d_{mob}>350 nm) is insufficient.

124   The SP2 was developed on the basis of the laser-induced incandescence technique and

125   provides an advantage to the study of individual BC particle properties, including mass,

126   size and mixing state. The SP2 determines the refractory BC (rBC) mass from particle

127   to particle, thus provideing the masses of BC aggregates throughout a wide size range

128   (70–500 nm mass-equivalent diameter claimed by the manufacturer) with high

129   sensitivity and accuracy (Schwarz et al., 2006). Recently, a tandem system consisting

130   of an SP2 connected next to a DMA was developed to study the properties of size-

131   resolved BC aerosols in the atmosphere. The mass distributions and mixing states of

132   the size-selected BC were investigated in northern India by using a DMA-SP2 tandem

133   system (Raatikainen et al., 2017). Coupling an SP2 with a volatility tandem DMA

134   (VTDMA), rBC core size distributions of internally mixed BC and those measured by

135   the VTDMA were compared at the prescribed mobility size ranges. Subsequently, the

136   morphology and effective density of the internally mixed BC particles were studied

137   (Zhang et al., 2016). The hygroscopic properties of BC particles were studied by using

138   a hygroscopicity tandem DMA (HTDMA)-SP2 coupling system (McMeeking et al.,

139   2011; Liu et al., 2013). Few studies have been performed on the morphology and

140   effective density of fractal-like BC aggregates uncoated by other components using the

141   DMA-SP2 measurement, especially in the ambient atmosphere.

142   Using the DMA-SP2/CPC system, Gysel et al. (2012) revealed that the SP2 was unable

143   to reliably detect BC particles from a PALAS spark discharge soot generator due to the

144   lower detection limit of the SP2 for loosely packed agglomerates made up of small

145   primary spherules (~5–10 nm in diameter). However, they also claimed that a well-

146   aligned SP2 was expected to have a detection efficiency adequate to measure the BC

147   aggregates (e.g., diesel exhaust soot) in the atmosphere because these BC aggregates

148   have larger primary spherules and substantially higher effective densities than the

agglomerates made up of small primary spherules. Therefore, in this study, a DMA-SP2 tandem system was built to examine the mass-mobility relationship (from which the morphology and effective density were further derived) of uncoated BC aggregates, especially in the large particle size range (e.g., d_{mob}>350 nm) which was seldom included in previous tandem measurements. Moreover, the uncoated BC aggregates were distinguished from the thickly-coated BC particles by using the SP2, allowing the study on the mass-mobility relationship of ambient BC aggregates in different atmospheric environments. Previous DMA-ELPI or APM tandem measurements were mainly conducted in the laboratory or in the source environments (e.g., in the tunnel) where fresh BC aggregates were predominant.

Beijing, the capital of China, has suffered from severe air pollution issues in recent years. Studies have revealed that emissions from coal combustion and/or biomass burning for industry activities and residential heating have played a predominate role in the particulate pollution in Beijing, especially in the polluted episodes (Zhang et al., 2013; Huang et al., 2014; Wu et al., 2017; Ma et al., 2017a,b). Thus, the variation in the mass-mobility relationship of uncoated BC aggregates was also compared for a polluted episode and a clean episode to examine the possible influence of source change on the morphology of these BC aggregates. In addition, a better mobility size resolution (33 logarithmic size bins from 20 to 750 nm) was set for our DMA-SP2 system than that used in previous similar studies in which only a few mobility diameters in the range of ~150–350 nm were selected (Zhang et al., 2016; Liu et al., 2013; McMeeking et al., 2011). Similar to the study presented in Raatikainen et al. (2017), the high size resolution provides an advantage for calculating the BC mass and number size distribution in the polluted region in our future studies.

2 Measurements

2.1 Experimental setup

A tandem system comprises a size selection unit and a measurement section was built and deployed in an ambient experiment that was conducted on the roof of a building (approximately 8 m above the ground) on the campus of the Institute of Atmospheric

Physics, Chinese Academy of Sciences (IAP, CAS) during the winter from 23 January to 10 February 2018 (19 days in total). The site is located in an urban area of Beijing; it is a few hundred meters away from two main roads and thus may be significantly affected by vehicle emissions. More information about the measurement site is described in previous studies (e.g., Wu et al., 2016, 2017).

As shown in Fig. 1, polydisperse aerosols in the sample air were drawn through the size selection unit (a model 3087 neutralizer, a model 3080 classifier and a model 3081 DMA, TSI Inc., Shoreview, MN, USA) to generate quasi-monodisperse particles with a certain electrical d_{mob}. Before entering the system, the ambient air was dried prior to passing through a 12-inch-long Nafion dryer (model MD-700-12F-3, Perma Pure LLC, Toms River, NJ, USA). A vacuum pump was used to draw the dry sheath air (e.g., particle-free indoor air) opposite to the flow direction of the sample air to provide an appropriate vacuum degree required for the dryer. The size-selected particles were delivered to the measurement section for analysis by various methods, including an SP2 (Droplet Measurement Technologies, Boulder, CO, USA), a CPC (model 3776, TSI Inc., Shoreview, MN, USA) and two microaethalometers (model AE51, AethLabs, San Francisco, CA, USA). The operational flow rates were set to 0.1, 0.3 and 0.15 LPM (STP) for the SP2, CPC and two AE51s, respectively. The sheath flow rate was set to 3 LPM, resulting in a ratio of sheath-to-sample flow rate of 4.3:1 for the DMA. Particles in the range of 15–750 nm in mobility diameter could be selected. The flow rate for each instrument was calibrated using a soap film flowmeter (model Gilian Gilibrator-2, Sensidyne, Petersburg, FL, USA) before the experiment to ensure the accuracy of the selected particle sizes and measurements. The scientific purpose of this experimental setup was to study the mixing states of size-selected BC particles, the mass and number size distribution of BC, as well as the morphology and effective density of the uncoated BC aggregates that are discussed in the current study. Since only the DMA and SP2 were involved in the measurements presented in this study, the setting and operation of the two instruments were described and discussed in detail.

208
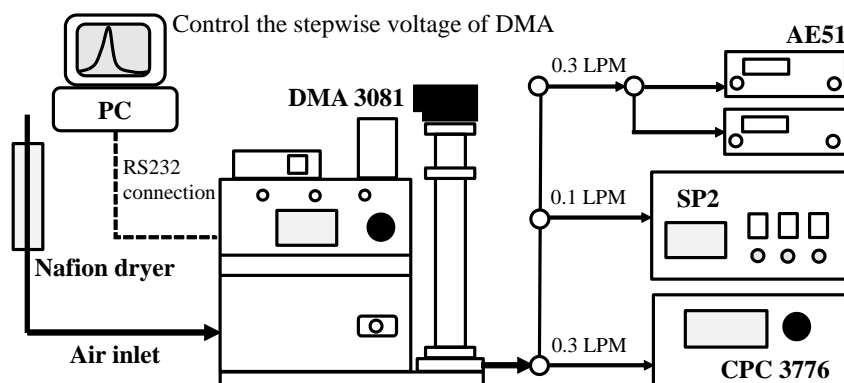
209 Fig. 1 Schematic of the experimental setup for size-resolved measurements of black

210 carbon.

211

2.2 Particle size selection

213 The DMA was connected to an external computer on which a program was run to

214 control the voltage of the DMA, i.e., the particle mobility diameter (d_{mob}). Thirty-three

215 mobility diameters were set in the program to cyclically control the particles selected

216 by the DMA and gradually increased from 20 nm to 750 nm at the logarithmic scale.

217 Stepwise size selection was repeated until the operator stopped the program. A short

218 cycle with each of the 33 diameters lasting for 18 s and a long cycle with each size

219 lasting for 36 s were set to alternately operate in this experiment (Fig. S1 in the

220 supplemental file). The purpose of this setting was to identify the time difference

221 between the size selection and the subsequent measurement, as described in the

222 following sections.

223

2.3 Black carbon measurement

225 The individual particulate rBC mass was measured by the SP2 according to the laser-

226 induced incandescence signal when the particle passed through the intense Nd:YAG

227 intracavity continuous laser beam (Schwardz et al., 2006) with a Gaussian distribution.

228 The rBC mass in the SP2 detection range (~0.3–250 fg in this study, dependent on the

229 laser intensity of a specific instrument) is proportional to the peak of the incandescence

230 signal independent of the mixing state of the BC particles. If a BC particle is coated

231 with nonrefractory components, the coating will evaporate before the rBC core

232   incandesces, leading to a time lag between the peaks of incandescence and scattering

233   signals that are synchronously detected by the SP2 (Moteki and Kondo, 2007).

234   According to the frequency distribution of the time lag, there was a significant

235   distinction between thickly-coated (i.e., internally mixed) BC particles (*int*BC) and

236   thinly-coated or uncoated (i.e., externally mixed) BC particles (*ext*BC) (Fig. S2) with a

237   minimum frequency at ~2 μs. BC-containing particles with delay times shorter than 2

238   μs were identified as *ext*BC. The delay time threshold might vary slightly from one SP2

239   to another, e.g., Zhang et al. (2016) reported a short time lag of 1.6 μs. However, the

240   delay time threshold should be constant for a given instrument. In previous

241   measurements using the same SP2 employed in this study, the critical delay time was

242   maintained at 2 μs regardless of the ambient conditions, such as the pollution level (Wu

243   et al., 2016, 2017). A fraction of BC-containing particles with thin or even moderate

244   coatings might also be recognized as *ext*BC using the time-delay approach (Laborde et

245   al., 2012). The effects of these thinly or even moderately coated BC particles will be

246   discussed in Section 3.2 by reducing the delay time threshold from 2 μs to 1.2 μs and

247   0.4 μs, respectively.

248   The scattering signal of a single particle synchronously detected by the SP2 can be used

249   to estimate the optical size of the particle. The mixing state of a BC-containing particle

250   can be deduced by comparing the optical size of the particle and the mass-equivalent

251   size of the rBC core. Since the nonrefractory coating of a BC-containing particle is

252   evaporated due to the light absorption and heating of the rBC core when it passes

253   through the laser beam, the scattering cross-section of this particle, which is

254   proportional to the scattering intensity at a given incident light intensity, is gradually

255   decreased. To estimate the initial optical size of this particle, an approach called

256   leading-edge-only (LEO) fitting was developed (Gao et al., 2007). A small fraction of

257   the measured scattering signal at its initial stage before the particle is perturbed by the

258   laser is employed in the LEO fitting to reconstruct the expected scattering distribution

259   of the initial particle. In this method, the location of the leading edge in the beam is also

260   required, which is determined from a two-element avalanche photodiode (APD) signal.

261   Unfortunately, the notch in the two-element APD of our SP2 failed to fix in an adequate

position (e.g., before the peak location of the laser beam) in this experiment. Thus, the optical size and the consequent coating thickness of the BC-containing particle cannot be estimated. However, the coating thickness is not a crucial quantity in our current study on the morphology and density of uncoated BC aggregates. The coating thickness can provide a validation of our discrimination of *ext*BC but should have little influence on our final analysis and the discussion presented in the following sections.

Before the experiment, the incandescence signal was calibrated using DMA-selected monodisperse Aquadag particles. The effective densities of the mobility size-selected Aquadag particles were referred to the polynomial equation as a function of the d_{mob} reported in Gysel et al. (2011). The incandescence signal is more sensitive to the Aquadag particles than to the ambient BC particles, i.e., the Aquadag particle induces a higher incandescence signal peak (by a factor of ~25%) than fullerene soot or an ambient BC particle with the same mass (Laborde et al., 2012). Thus, the peak intensity of the incandescence signal was reduced by a factor of 25% when calculating the calibration coefficient. The same calibration was performed again after the experiment. The calibration factors varied little (<3%), indicating the stability of the SP2 measurement during the entire experiment (Fig. S3). The uncertainty in the individual rBC mass determination is estimated to be ~10% due to the uncertainties in the rBC mass calibration and the effective density of the calibration material. An additional uncertainty may also arise in the determination of *ext*BC masses when the time-delay approach is used to distinguish the mixing state of BC particles. The uncertainty will be further discussed in Section 3.2.

3 Data processing

3.1 Identifying the time difference between the size selection and the SP2 measurement

There exists a considerable difference between the time recorded by the size selection program and that recorded by the SP2, due to the time cost of the particles transmitting from the DMA to the SP2, as well as the system clock difference between the computer on which the size selection program runs and that for the SP2 data acquisition. As

shown in Fig. S1, the SP2 measurement occurs significantly later than the size selection. We develop two methods to identify the time difference. The first method is to find the time difference between the local peak in the particle number concentration (including both scattering and incandescence) detected by the SP2 and the beginning of the corresponding size selection cycle. During the experiment, stepwise size selection was cyclically performed to produce quasi-monodisperse particles with sizes gradually increasing from 20 nm to 750 nm. Thus, at the beginning of each new cycle, the voltage of the DMA should first drop drastically from a high value to a low one to make the particle size decrease from 750 nm to 20 nm. As a result, some particles with sizes in the SP2 efficiently detectable range (~100–500 nm) are measured during the descent period, producing a local peak in the number concentration. Since it takes only a few seconds for the descent, identifying the occurrence time of the local peak position in the SP2 clock and the beginning time of the size selection in the external computer clock will provide the time difference of each cycle.

The other method is to check the consistency of the number and/or mass size distributions between the short-duration cycle and long-duration cycle. Although the durations of each size in the short cycle and long cycle are different (18 s vs. 36 s), the time difference between the size selection and the measurement should be uniform for adjacent short and long cycles. Setting an initial time difference and calculating the mean number and/or mass concentration of each particle size, the number and/or mass size distributions are obtained. Then, the correlation coefficients between the size distributions during short and long cycles are calculated. Changing the time difference gradually, we can obtain a set of correlation coefficients as functions of the time differences. The time difference resulting in the maximum correlation coefficient is considered the difference between the size selection and the measurement.

Since the detection efficiency of the SP2 decreases dramatically in the small particle range (Fig. S4), the size distributions of the SP2-detected particles are inadequate for further calculation of the correlation coefficients. Therefore, the former method was employed in current study to identify the time difference between the size selection and the SP2 measurement. The latter method will be used to examine the time difference

322   between the size selection and the AE51/CPC measurements in our future study on the

323   number and mass size distributions of BC.

324

325   **3.2 Determination of the typical masses of extBC at prescribed mobility sizes**

326   Particles in a certain size range are selected by the DMA instead of absolutely

327   monodisperse particles at a given mobility size due to the effect of the transfer function.

328   In addition, larger particles with multiple charges are also selected. The frequency and

329   number size distributions of *ext*BC as a function of the mass-equivalent diameter of

330   rBC (d_{me}) at different mobility sizes are presented in Fig. S5 and S6, respectively. Note

331   that the number size distribution has been normalized by the peak value of the

332   corresponding distribution. Since the frequency and number size distributions of *ext*BC

333   are quite insufficient at small particle sizes ($d_{me}<70$ nm) due to the low detection

334   efficiency of the SP2 (Fig. S4), only the distributions with a d_{mob} larger than 140 nm

335   are presented. In our following study, we mainly address the morphology and effective

336   density of *ext*BC in the 140–750 nm d_{mob} range. The normalized number size

337   distributions at five representative d_{mob} (e.g., 140, 225, 350, 500, 750 nm) are also

338   shown in Fig. 2. The *ext*BC particles having a considerable d_{me} range were observed

339   for a certain d_{mob}, indicating a wide transfer function of the DMA due to the relatively

340   low ratio of sheath-to-sample flow (4.3:1). Multicharged particles also affected the size

341   distribution, especially in the d_{mob} range of 100–400 nm (Ning et al., 2013). As shown

342   in Fig. S6 and Fig. 2, a minor peak is obviously observed at the right tail of the major

343   peak at each size distribution with a $d_{mob}<350$ nm.

344   As mentioned above, a fraction of thinly and/or moderately coated BC particles might

345   also be recognized as *ext*BC according to the time delay between the SP2 incandescence

346   and scattering signal peaks. These particles also have impacts on the size distribution

347   of *ext*BC at a given mobility size. A thinly-coated BC particle can be expected to have

348   a larger mass than a bare BC with the same mobility due to the restructuring of the

349   thinly coated BC particle by coating materials. These thinly coated BC particles will

350   increase the size distribution at their right tail when mixed with the effect of

351   multicharged particles. It is difficult or even impossible to separate the effects of the

thinly coated and multicharged particles based on the size distribution of extBC at the current stage. To examine the possible effect of these thinly coated particles, we tightened the criterion of the delay time for the discrimination of extBC, gradually decreasing from <2.0 μs to <1.2 μs and <0.4 μs. As shown in Fig. S5 and S6, a decrease in the delay time threshold results in a significant reduction in the data volume used in the analysis but has few effects on the major peak location of the distribution, which is used as the typical d_{me} of extBC at a given mobility size. The typical d_{me} values, determined as the mode values of the lognormal function that are employed to fit the major peak of the size distribution at a certain mobility size, vary little with the delay time thresholds (Table S1). The maximum discrepancy in the d_{me} is <3% throughout the prescribed mobility size range in this study (140–750 nm). The delay time threshold-caused change mainly appears at the right tail of the normalized number size distribution. Reducing the delay time threshold to 0.4 μs results in a significant decrease in the fraction of particles with a large d_{me} compared to the 2.0 μs and 1.2 μs thresholds (Fig. S6). These large particles are likely attributed to thinly and/or even moderately coated BC particles whose structures are relatively more compact than the absolutely bare BC particles. Therefore, we propose that thinly and/or even moderately coated BC and multicharged particles should both have effects on the size distribution of extBC, mainly at its right tail, while having little influence on the typical d_{me} that is considered as the peak d_{me} of the distribution at a given mobility size. The uncertainty in the typical d_{me} due to the time-delay approach that was utilized to distinguish the extBC is approximately 3% at a given d_{mob}, which is in turn ~10% in the corresponding mass of extBC. Combining the uncertainty in the rBC mass determined by the SP2 (~10%), the total uncertainty in the determined mass of extBC should be ~20% in the studied mobility range of 140–700 nm. For the adequate data volume used in the analysis, the results and discussion presented in the following sections are based on the database of extBC discriminated as BC-containing particles with delay times lower than 2.0 μs, unless otherwise specified.

381
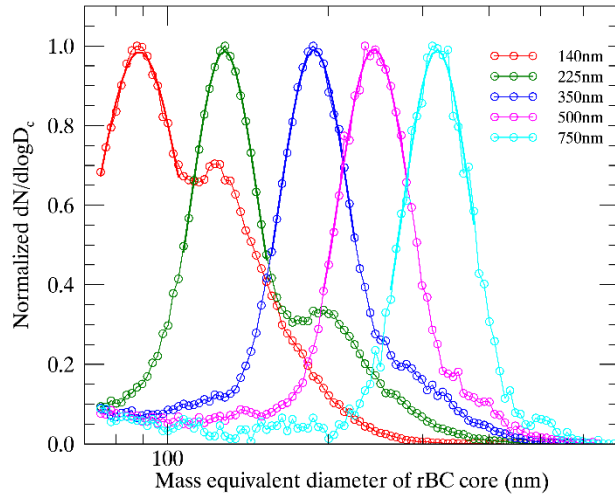
Fig. 2 Campaign average number size distribution of the mass-equivalent diameter of the rBC core of *ext*BC normalized by the peak value at five represented mobility diameters (140, 225, 350, 500 and 750 nm) selected by the DMA. Lognormal fitting is performed for the major peak of each distribution.

3.3 Theoretical calculation of the morphology and effective density

The structure of *ext*BC, agglomerated by primary spherules with diameters of 20-60 nm (Alexander et al., 2008), can be characterized by its mass-mobility relationship, which is approximately expressed as a power-law relationship between the mass of the agglomerate particle (m) and its mobility diameter (d_{mob}), expressed as

$$m = k \cdot d_{mob}^{D_{fm}} \tag{1}$$

where the prefactor k is a constant and D_{fm} is the mass-mobility scaling exponent, which was sometimes erroneously called the 'fractal dimension' in previous studies (e.g., Park et al., 2003). This quantity corresponds well to the virtual D_f and represents the morphology of the BC aggregates (Sorensen, 2011). The D_{fm} value of a sphere is 3. Thus, the morphology of a particle becomes increasingly closer to that of a sphere as the D_{fm} increases gradually to 3.

The effective density (ρ_{eff}) of the *ext*BC particles is calculated as the ratio of the BC mass (m) measured using the SP2 and the BC volume, which is based on the d_{mob} selected by the DMA, expressed as

402 $\rho_{eff} = \frac{6m}{\pi d_{mob}^3}$ (2)

403 Combining Eq. 1 and 2, ρ_{eff} can also be expressed as a function of d_{mob},

404 $\rho_{eff} = K \cdot d_{mob}^{D_{fm}-3}$ (3)

405 where K is a constant, corresponding to the prefactor k in the mass-mobility relationship.

406 The dynamic shape factor is also calculated to indicate the morphology of the extBC

407 particles. It is derived from the ratio of the slip-corrected mass-equivalent diameter (d_{me})

408 and d_{mob}, expressed as

409 $\chi = \frac{d_{mob} \cdot C_c(d_{me})}{d_{me} \cdot C_c(d_{mod})}$ (4)

410 where d_{me} is calculated from the BC mass (m) by assuming the BC particle to be a

411 compact sphere with a density of 1.8 g cm^{-3} (Taylor et al., 2015), and C_c is the

412 Cunningham slip correction factor parameterized by particle diameter (d)

413 $C_c(d) = 1 + \frac{2\lambda}{d}[\alpha + \beta\exp(-\frac{\gamma \cdot d}{2\lambda})]$ (5)

414 where λ is the mean free path of the gas molecules, which is set to 65 nm in this study

415 according to Zhang et al. (2016). The values of the three empirical parameters α, β and

416 γ are 1.257, 0.4 and 1.1, respectively (Eq. 9.34 on page 407 in Seinfeld and Pandis,

417 2006).

418

419 **4 Results and discussion**

420 **4.1 Mass-mobility relationship of the ambient extBC**

421 A power-law relationship was applied to the d_{mob}-determined extBC mass values,

422 delivering the mass-mobility scaling exponent (D_{fm}) of the ambient extBC (Fig. 3). In

423 the d_{mob} range of 140–750 nm, the fitted D_{fm} is 2.34, with one standard deviation of

424 0.03. The fitted D_{fm} is close to the lower limit of the D_{fm} values of diesel exhaust

425 particles presented in the literature, indicating the dominant contribution of diesel

426 exhaust to the extBC in our measurement site in urban Beijing. Depending on the fuel

427 type, engine type and load, the D_{fm} of diesel exhaust particles measured by the DMA-

428 APM or DMA-ELPI systems ranged between 2.22 and 2.84 (Olfert et al., 2007; Maricq

429 and Xu, 2004; Park et al., 2003 and references therein). The higher D_{fm} values in the

literature are likely attributed to the higher fraction of volatile and/or semivolatile components (e.g., sulfate) in the diesel exhaust (Park et al., 2003; Olfert et al., 2007). Accompanied by these volatile and/or semi-volatile components would result in a more compact structure of the particle, leading to a higher D_{fm} value compared to the bare BC aggregate. Since the rBC mass instead of the whole particle mass of *ext*BC was measured by the SP2, the relatively low D_{fm} was expected and reasonable in this study. In addition, the relatively low D_{fm} value observed in urban Beijing is also likely to imply high fuel quality (e.g., low sulfur content) and efficient combustion in vehicle engines, which decrease the organic and/or inorganic fractions in diesel exhaust particles. The D_{fm} value for the ambient soot agglomerates measured with a DMA-APM system near a diesel truck-dominated highway was 2.41 (Geller et al., 2006), slightly higher than the value in our study.

According to Sorensen (2011), the ideal fractal-like DLCA with a virtual D_f of approximately 1.78 should have an expected $D_{fm} \approx 2.2$ in the slip flow regime in which the BC aggregates are generally observed. The slightly larger D_{fm} value of ambient *ext*BC (2.34) in the current study might indicate a more compact structure than the ideal fractal-like DLCA due to the reconstruction effect by other components in the atmosphere. The reconstruction effect appears to be more significant in the smaller particle range than in the larger particle range. The smaller BC particles are more likely to be coated by volatile and/or semivolatile materials, which will be discussed in detail in the next section. We piecewise fitted the mass-mobility relationship using the power law function in the mobility ranges of 140–350 nm and 350–750 nm. A D_{fm} of 2.51±0.04 that was obtained in the smaller mobility range (140–350 nm) was obviously larger than the fitted value in the whole size range (140–750 nm). In contrast, a much lower D_{fm} with value of 2.07±0.02 was observed in the larger mobility range (350–750 nm). These results indicate that the ambient *ext*BC particles with larger mobility diameters were likely less influenced by the reconstruction effect than those with smaller mobility diameters.

459
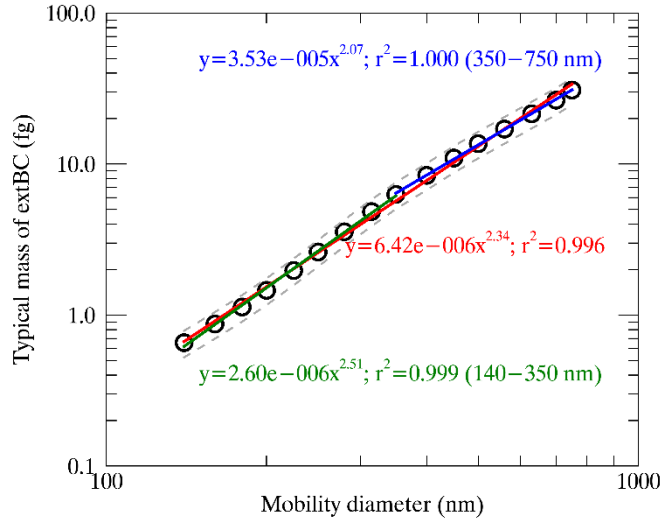
460 Fig. 3 The mass of *ext*BC particles as a function of the mobility diameter in the range

461 of 140–750 nm (black circles), fitted by a power-law relationship (red line). The power

462 law functions piecewise fitted in the 140–350 nm mobility range (green line) range and

463 in the 350–750 nm mobility range (blue line) are overlaid. The dashed lines represent

464 in the uncertainties in the determined *ext*BC masses.

465

466 Table 1 The typical mass-equivalent diameters (d_{me}) and corresponding masses of *ext*BC

467 at different mobility sizes (d_{mob}) selected by the DMA in the whole campaign, in a

468 polluted episode and in a clean period. The effective densities (ρ_{eff}) and dynamic shape

469 factors (χ) at the d_{mob} selected by the DMA in the whole campaign are also presented.

d_{mob} (nm)	d_{me} (nm)			mass (fg)			ρ_{eff} (g cm^{-3})	χ
	total	polluted	clean	total	polluted	clean		
140	88.8	87.2	88.5	0.66	0.63	0.65	0.46	2.16
160	97.5	96.9	98.1	0.87	0.86	0.89	0.41	2.27
180	106.2	106.1	107.0	1.13	1.13	1.15	0.37	2.35
200	115.6	116.1	115.5	1.46	1.48	1.45	0.35	2.40
225	127.9	128.6	128.4	1.97	2.01	1.99	0.33	2.41
250	140.5	142.2	141.0	2.62	2.71	2.64	0.32	2.41
280	155.8	158.0	154.4	3.56	3.72	3.47	0.31	2.41
315	172.6	174.8	170.6	4.85	5.04	4.68	0.30	2.40
350	188.2	191.8	185.9	6.28	6.65	6.05	0.28	2.41
400	207.4	213.7	207.4	8.41	9.20	8.41	0.25	2.43
450	226.4	232.3	225.9	10.94	11.81	10.87	0.23	2.50
500	243.8	251.4	242.2	13.65	14.98	13.39	0.21	2.62
560	262.6	271.1	260.1	17.06	18.77	16.58	0.19	2.71
630	283.2	293.5	282.5	21.42	23.83	21.25	0.16	2.81

| 700 | 305.1 | 312.7 | 305.0 | 26.76 | 28.83 | 26.73 | 0.15 | 2.89 |
| 750 | 319.6 | 328.8 | 323.5 | 30.76 | 33.49 | 31.92 | 0.14 | 2.93 |

470

471   The variation in the morphology of *ext*BC was further examined by comparing the

472   mass-mobility relationship in a polluted episode and in a consecutively clean period.

473   As shown in Fig. S7, a polluted episode rapidly formed at 14:00 (local time, if not

474   specified) on 26 January and lasted one and a half days to 0:00 on 28 January 2018.

475   The mean $PM_{2.5}$ mass concentration was 72.1 ± 23.1 µg m^{-3} in this polluted episode,

476   three times the campaign average value (23.0 ± 26.7 µg m^{-3}). The D_{fm} value is 2.42 ± 0.09

477   in the polluted episode, higher than that (2.33 ± 0.06) observed in the consecutively clean

478   period from 1:00 on 28 January to 18:00 on 31 January 2018, during which the average

479    $PM_{2.5}$ concentration was merely 8.9 ± 2.7 µg m^{-3} (Fig. S8). The higher D_{fm} in the polluted

480   episode is mainly due to the increase in the masses of *ext*BC at large mobility sizes (e.g.,

481    $d_{mob} > 250$). As shown in Table 1, the typical masses of *ext*BC in the 280–700 nm d_{mob}

482   range in the polluted episode are ~7–13% larger than those in the clean period.

483   Although the differences might result from the uncertainty (~20%) in the mass

484   determination of *ext*BC, the commonly larger *ext*BC masses (in the 280–700 nm d_{mob}

485   range) to some degree still imply a possibly more compact structure of *ext*BC

486   aggregates in the polluted episode, which might relate to changes in the dominant

487   sources and the ambient environment. Previous studies have revealed that regionally

488   transported pollutants emitted from coal combustion and/or biomass burning played an

489   important or even predominant role in polluted episodes in Beijing (Wu et al., 2017;

490   Ma et al., 2017a). Thus, a considerable fraction of *ext*BC aggregates from these sources

491   is likely to coexist with the local vehicle-emitted BC aggregates in the polluted episode,

492   even though the proportion of *ext*BC in the total BC-containing particles decreased (Fig.

493   S9). These transported BC aggregates originating from coal combustion and/or biomass

494   burning might have a more compact structure than those from vehicle exhaust due to

495   the differences in the combustion environments and efficiencies. In addition, the BC

496   aggregates might also become more compact due to the reconstruction effect by the

497   volatile and/or semivolatile components which are generally abundant in polluted

498   episodes. Both possible factors are likely to result in the larger D_{fm} values in the polluted

499   episode.

500

4.2 Size-resolved effective densities of the ambient *ext*BC

502   In contrast to the mass of *ext*BC (m), the effective density of the *ext*BC particles (ρ_{eff})

503   showed a significant decreasing trend as the d_{mob} increased from 140 nm to 750 nm

504   (Fig. 4 and Table 1). The highest ρ_{eff} of 0.46 g cm^{-3} was observed in the 140 nm d_{mob},

505   likely because the BC aggregates at the smallest size are made up of the fewest primary

506   spherules. When the d_{mob} increased to 750 nm, ρ_{eff} decreased to as low as 0.14 g cm^{-3},

507   approximately one-third of that at 140 nm. The very low ρ_{eff} values agree well with the

508   fractal-like nature of the *ext*BC particles.

509

510
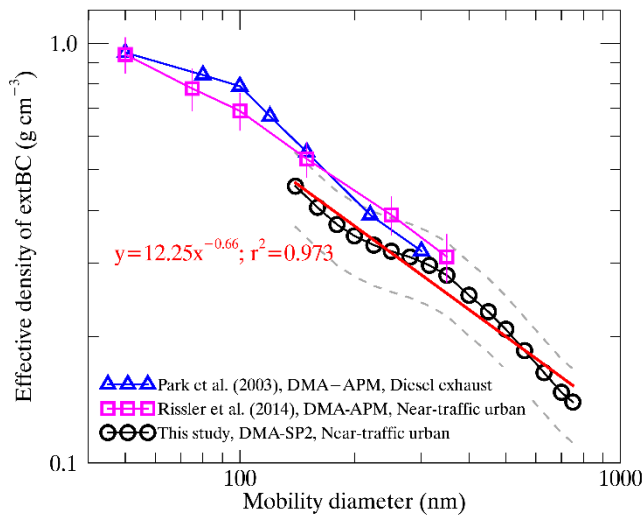
511   Fig. 4 The effective density (ρ_{eff}) of the *ext*BC particles as a function of the mobility

512   diameter (d_{mob}) (black circles). The red line represents the power-law fitting of ρ_{eff}

513   against d_{mob}. The variations of ρ_{eff} with d_{mob} measured for the soot agglomerates from

514   diesel exhausts (Park et al., 2003) and near-traffic urban environments (Rissler et al.,

515   2014) are also presented as blue triangles and red squares, respectively. The dashed

516   lines represent in the uncertainties in the determined ρ_{eff}.

517

518   The ρ_{eff} values obtained by the DMA-SP2 measurements are close to those of the lower

519   limits of diesel exhaust particles measured by the DMA-APM (or CPMA) or DMA-

520   ELPI systems. Park et al. (2003) reported a decrease in the ρ_{eff} of diesel exhaust particles

521   under a moderate (50%) engine load from 0.95 g cm^{-3} to 0.32 g cm^{-3} as the mobility

522   diameter increased from 50 nm to 300 nm (Fig. 4). The ρ_{eff} values presented in Park et

523   al. (2003) are approximately 1.25, 1.18 and 1.05 times those in our study at ~150 nm,

524   220 and 300 nm in mobility diameter, respectively. The differences in ρ_{eff} values

525   between our study and the literature are generally within the uncertainty (~20%) in the

526   mass determination of *ext*BC at prescribed mobility sizes. However, the commonly

527   lower ρ_{eff} values are also likely due to the techniques used to determine the mass of BC

528   aggregates. Some previous studies on the ρ_{eff} of diesel exhaust particles using the DMA-

529   APM or DMA-ELPI tandem measurements also showed a slightly larger ρ_{eff} throughout

530   the comparable mobility ranges (e.g., ~150–350 nm) than that measured in this study

531   (Maricq and Xu, 2004; Olfert et al., 2007). The masses of the bare BC particles were

532   determined by the laser-induced incandescence technique of the SP2. In a previous

533   tandem system, the APM (or CPMA) or ELPI was utilized to determine the typical

534   mass of BC aggregates at a given mobility, and the BC aggregates are likely composed

535   of a fraction of volatile and/or semivolatile components in addition to the bare primary

536   particles. These volatile and/or semivolatile components increase the mass of the whole

537   particle, resulting in a larger ρ_{eff} value at a certain mobility and cause a compact

538   structure of the BC aggregate. For example, Olfert et al. (2007) found that the ρ_{eff} of

539   diesel exhaust particles coated with minor sulfate and water contents (~2% of the total

540   particle mass) was ~0.4 g cm^{-3} at 299 nm, only slightly larger than the value of diesel

541   exhaust particles (0.32 g cm^{-3}) measured in Park et al. (2003) and that of *ext*BC in the

542   urban atmosphere (0.31 g cm^{-3}) in our study at the same mobility size. However, the ρ_{eff}

543   value increased significantly to ~0.71 g cm^{-3} at a relatively high engine load of 40%

544   due to the high sulfate levels (~30% of the total particle mass) in the diesel exhaust

545   particles (Olfert et al., 2007).

546   The ρ_{eff} of ambient soot aggregates also showed a similar decreasing trend with

547   increasing d_{mob} based on the DMA-APM system (Geller et al., 2006; Rissler et al.,

548   2014). Rissler et al. (2014) showed a decrease in the average ρ_{eff} of BC aggregates from

549   0.94 g cm^{-3} to 0.31 g cm^{-3} in the near-traffic urban environment as the d_{mob} increased

from 50 nm to 350 nm (Fig. 4), similar to that of the freshly emitted diesel exhaust particles presented in Park et al. (2003). However, based on the same method, the ρ_{eff} values of the ambient BC aggregates that mostly originated from diesel exhausts (Geller et al., 2006) are substantially different from those presented in Rissler et al. (2014), especially in the large particle size range. The ρ_{eff} at ~350 nm was 0.17 g cm^{-3} in Geller et al. (2006), approximately half of the value presented in Rissler et al. (2014). The reason for the discrepancy might be related to the large measurement uncertainties of the DMA-APM system for large particles, e.g., with sizes greater than 300 nm in the d_{mob}, since these large particles are less abundant in the ambient atmosphere (Geller et al., 2006). Compared to the results presented in Rissler et al. (2014), the ρ_{eff} values of ambient extBC aggregates in our study are slightly lower, e.g., by ~17%, ~18% and ~6% in 150 nm, 250 nm and 350 nm d_{mob}, respectively. The relatively higher ρ_{eff} values are also likely attributed to the effects of volatile and/or semivolatile components in the soot aggregates. Rissler et al. (2014) found that the residual mass fraction of volatile and/or semivolatile materials in the soot aggregates was ~10%, even when the sample air was heated to 300 °C before entering the system for measurement.

It is interesting to note that the ρ_{eff} values appear to be closer to the values presented in the literature using the DMA-APM measurements in the 280–350 nm d_{mob} range (Fig. 4). As shown in Fig. 3, larger typical masses of extBC in this range are also observed beyond the logarithmic scaled linear curve that is fitted to the mass-mobility relationship. The relatively larger masses and ρ_{eff} values might imply a more compact structure of extBC aggregates in this range which is likely resulted from the reconstruction effect by the ambient volatile and/or semivolatile components. As shown in Fig. S9, the size-resolved number fractions of extBC exhibit a minimum in the 280–350 nm d_{mob} regardless of whether they are associated with the polluted episode or the clean period. This finding indicates that particles in this mobility range are more likely to be thickly coated by other components compared to those in the smaller or larger mobility ranges. Zhang et al. (2016) also observed an increased coating thickness of the BC-containing particles in the mobility range of 200–350 nm (Table 1 in the literature) using the VTDMA-SP2 measurement at a suburban site ~70 km away from our

580   observation site, although the variation in the coating thickness in the larger mobility

581   range was not investigated. It should be noted that the number fraction of *ext*BC at each

582   mobility size presented in Fig. S9 is roughly calculated as the ratio of the *ext*BC number

583   concentration to the sum of *ext*BC and *int*BC, in which the multiply charged effects

584   were not corrected. Although the *ext*BC particles without and/or with thin coatings are

585   the focus of the current study, the higher fraction of thickly coated BC particles in the

586   280–350 nm d_{mob} range implies a higher possibility that these *ext*BC particles in the

587   same range were affected by volatile and/or semivolatile materials in the atmosphere,

588   in turn resulting in a more compact structure of these BC aggregates. Further detailed

589   studies of the size distribution of BC (including *ext*BC, *int*BC and both) and non-BC

590   particles based on the combined measurements of SP2 and CPC are needed in our

591   further work to reveal the potential mechanism for this phenomenon.

592   Although the ρ_{eff} of *ext*BC at small sizes ($d_{mob}<140$ nm) cannot be determined due to

593   the lower limit of the DMA-SP2 system, we extended the ρ_{eff} of *ext*BC to a large size

594   range ($350<d_{mob}<750$ nm), which was barely investigated in previous studies using

595   tandem measurements. A continuous decrease in ρ_{eff} with increasing d_{mob} was observed

596   even in the large size range between 350 nm and 750 nm (Fig. 4). It is reasonable to

597   infer that the structure of the *ext*BC particles becomes looser when the fractal-like

598   aggregates built up by the primary spherules increase.

599

4.3 Dynamic shape factors of the ambient *ext*BC

601   Due to their fractal-like structures, the *ext*BC particles generally have large dynamic

602   shape factors (χ) with values in the range of 2.16 to 2.93 (Table 1), much larger than

603   those of *int*BC with an average value of ~1.2 (Zhang et al., 2016). The χ value declined

604   exponentially as a function of coating thickness of BC-containing particles (Zhang et

605   al., 2016). In contrast to the decrease in ρ_{eff}, the χ values of *ext*BC generally increase as

606   the d_{mob} increases from 140 nm to 750 nm (Fig. 5). The *ext*BC particles 750 nm in

607   mobility diameter have a mean χ value of 2.93, approximately 1.36 times that for 140

608   nm d_{mob} particles (Table 1). The larger particles have looser structures, resulting in

609   higher χ values. However, the χ values appear to vary slightly in a narrow range between

2.40 to 2.41 in the size range of 200 nm to 350 nm (Fig. 5). The hiatus in the gradual increase in χ should also relate to the more compact structure of *ext*BC particles in the 280–350 nm mobility range, which has been discussed in detail in the previous sections. .
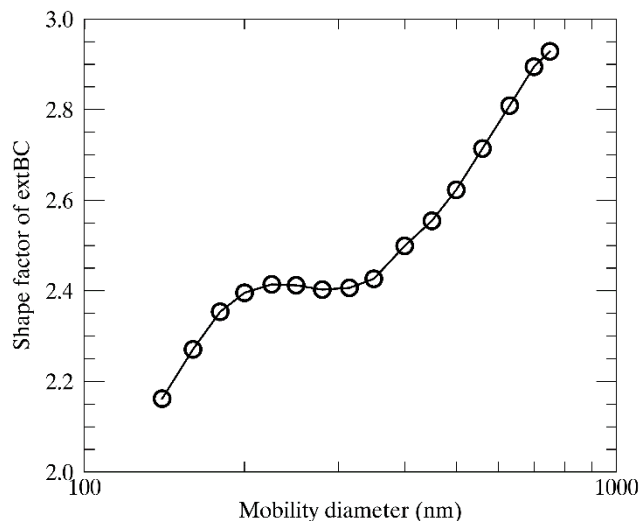
Fig. 5 The dynamic shape factor of the *ext*BC particles as a function of the mobility diameter in the range of 140–750 nm.

5 Conclusions

The DMA-SP2 system was established to study the morphology and effective density of the ambient *ext*BC particles, especially in the larger mobility size range, i.e., $350<d_{mob}<750$ nm, which was seldom investigated in previous tandem measurements. Quasi-monodisperse particles in the d_{mob} range of 20–750 nm were stepwise selected using the DMA and then delivered to the SP2 for rBC mass measurement and mixing state discrimination. The time difference between the size selection and the SP2 measurement was previously processed using the local peak approach. The normalized number size distribution of *ext*BC, distinguished as having a delay time between the incandescence signal peak and the scattering peak detected by the SP2 of less than 2 μs, as a function of d_{me} was investigated at each prescribed mobility size in the range of 140–750 nm. The size distributions at smaller mobility sizes were not presented due to the lower limit of the rBC mass determined by using the SP2. The peak d_{me}, calculated

as the mode value of a lognormal function fitted to the major peak of the size distribution, was determined as the typical d_{me} value at each mobility size. Consequently, the typical mass of *ext*BC at each mobility size was identified. Reducing the delay time threshold employed to discriminate the *ext*BC had few effects on the determined masses of *ext*BC, implying the reliability of our study for the *ext*BC particles. The uncertainty in the determined *ext*BC masses was ~20%, combining the uncertainty in the SP2-measured rBC mass with that related to the time-delay approach. On this basis, the mass-mobility relationship of ambient *ext*BC in urban Beijing was investigated. The campaign average D_{fm} value was estimated to be 2.34±0.03 by fitting the derived *ext*BC masses as a power-law function of d_{mob} in the range of 140–750 nm, close to the lower-limit D_{fm} value of diesel exhaust particles. A relatively larger D_f value was observed in the polluted episode than in the clean period (2.42±0.09 vs. 2.33±0.06), implying a more compact structure of BC aggregates in the polluted episode.

A decrease in ρ_{eff} with increasing d_{mob} was observed, with the ρ_{eff} value decreasing from 0.46 g cm^{-3} at 140 nm mobility to 0.14 g cm^{-3} at 700 nm. The ρ_{eff} values derived using the DMA-SP2 measurement were slightly lower than those based on the DMA-APM measurement. This difference was most likely due to the bias in the *ext*BC mass determination using the SP2 and APM techniques. The pure rBC mass determined using the SP2 in this study was generally lower than the total mass of the BC aggregate, which comprises both rBC and a possible fraction of nonrefractory components. The ρ_{eff} values in the 280–350 nm mobility range appeared to be much closer to the values for soot aggregates reported in the literature by using the DMA-APM tandem measurement. This finding might be related to the more compact structure of BC aggregates in this range, which was likely influenced by the reconstruction effect of volatile and/or semivolatile components in the atmosphere. The reconstruction effect might also result in a hiatus in the gradually increased χ value in the range of 200–350 nm. Large χ values generally increased from 2.16 to 2.93 with increasing d_{mob}, further implying the high fractal structure of *ext*BC particles.

Acknowledgments

This work was supported by the National Key Research and Development Program of China (no. 2017YFC0209601, 2017YFC0212701) and the National Natural Science Foundation of China (no. 41575150, 41775155, 91644217 and 91644219).

References

Alexander, D. T., Crozier, P. A., and Anderson, J. R.: Brown carbon spheres in East Asian outflow and their optical properties, Science, 321, 833–836, doi:10.1126/science.1155296, 2008.

Bi, L., Yang, P., Kattawar, G. W., Mishchenko, M. I.: Efficient implementation of the invariant imbedding T-matrix method and the separation of variables method applied to large nonspherical inhomogeneous particles, J. Quant. Spectrosc. Radiat. Transfer, 116, 169−183, doi:10.1016/j.jqsrt.2012.11.014, 2013.

Huang, R. J., Zhang, Y. L., Bozzetti, C., Ho, K.-F., Cao, J. J., Han, Y. M., Daellenbach, K. R., Slowik, J. G., et al.: High secondary aerosol contribution to particulate pollution during haze events in China, Nature, 514, 218–222, doi:10.1038/nature13774, 2014.

Huang, X. F., Sun, T. L., Zeng, L. W., Yu, G. H., and Luan, S. J.: Black carbon aerosol characterization in a coastal city in South China using a single particle soot photometer, Atmos. Environ., 51, 21–28, doi:10.1016/j.atmosenv.2012.01.056, 2012.

Gao, R. S., Schwarz, J. P., Kelly, K. K., Fahey, D. W., Watts, L. A., Thompson, T. L., Spackman, J. R., Slowik, J. G., Cross, E. S., Han, J.-H., Davidovits, P., Onasch, T. B., and Worsnop, D. R.: A novel method for estimating light-scattering properties of soot aerosols using a modified single-particle soot photometer, Aerosol Sci. Technol., 41, 125–135, doi:10.1080/02786820601118398, 2007.

Geller, M., Biswas, S., and Sioutas, C.: Determination of particle effective density in urban environments with a differential mobility analyzer and aerosol particle mass analyzer, Aerosol Sci. Technol., 40, 709–723, doi:10.1080/02786820600803925, 2006.

Gysel, M., Laborde, M., Olfert, J. S., Subramanian, R., and Gröhn, A. J.: Effective density of Aquadag and fullerene soot black carbon reference materials used for SP2 calibration, Atmos. Meas. Tech., 4, 2851–2858, doi:10.5194/amt-4-2851-2011, 2011.

Gysel, M., Laborde, M., Mensah, A. A., Corbin, J. C., Keller, A., Kim, J., Petzold, A., and Sierau, B.: Technical Note: The single particle soot photometer fails to reliably detect PALAS soot nanoparticles, Atmos. Meas. Tech., 5, 3099–3107, doi: 10.5194/amt-5-3099-2012, 2012.

IPCC: Summary for policymakers, in: Climate Change 2013: The Physical Science Basis. Contribution of Working Group I to the Fifth Assessment Report of the Intergovernmental Panel on Climate Change, edited by: Stocker, T. F., Qin, D., Plattner, G.-K., Tignor, M., Allen, S. K., Boschung, J., Nauels, A., Xia, Y., Bex, V., and Midgley, P. M., Cambridge University Press, Cambridge, United Kingdom and New York, NY, USA, 2013.

Jacobson, M. Z.: Strong radiative heating due to the mixing state of black carbon in atmospheric aerosols, Nature, 409, 695–697, doi:10.1038/35055518, 2001.

Khalizov, A. F., Xue, H. X., Wang, L., Zheng, J., and Zhang, R. Y.: Enhanced light absorption and scattering by carbon soot aerosol internally mixed with sulfuric acid, J. Phys. Chem. A, 113, 1066–1074, 2009.

Laborde, M., Mertes, P., Zieger, P., Dommen, J., Balternsperger, U., and Gysel, M.: Sensitivity of the Single Particle Soot Photometer to different black carbon types, Atmos. Meas. Tech., 5, 1031–1043, doi:10.5194/amt-5-1031-2012, 2012.

Liu, D., Allan, J., Whitehead, J., Young, D., Flynn, M., Coe, H., McFiggans, G., Fleming, Z. L., and Bandy, B.: Ambient black carbon particle hygroscopic properties controlled by mixing state and composition, Atmos.

Chem. Phys., 13, 2015–2029, doi:10.5194/acp-13-2015-2013, 2013.

Liu, D. T., Whitehead, J., Alfarra, M. R., Reyes-Villegas, E., Spracklen, D. V., Reddington, C. L., Kong, S. F., Williams. P. I., Ting, Y.-C., Haslett, S., Taylor, J. W., Flynn, M. J., Morgan, W. T., McFiggans, G., Coe, H., and Allan, J. D.: Black-carbon absorption enhancement in the atmosphere determined by particle mixing state, Nature Geoscience, 10, 184–188, doi:10.1038/NGEO2901, 2017.

Ma, Q. X., Wu, Y. F., Zhang, D. Z., Wang, X. J., Xia, Y. J., Liu, X. Y., Tian, P., Han, Z. W., Xia, X. A., Wang, Y., and Zhang, R. J.: Roles of regional transport and heterogeneous reactions in the PM2.5 increase during winter haze episodes in Beijing, Sci. Tot. Environ., 599–600, 246–253, doi:10.1016/j.scitotenv.2017.04.193, 2017a.

Ma, Q. X., Wu, Y. F., Tao, J., Xia, Y. J., Liu, X. Y., Zhang, D. Z., Han, Z. W., Zhang, X. L., and Zhang, R. J.: Variations of chemical composition and source apportionment of PM2.5 during winter haze episodes in Beijing, Aerosol Air Qual. Res., 17, 2791–2803, doi:10.4209/aaqr.2017.10.0366, 2017b.

Maricq, M. M., and Xu, N.: The effective density and fractal dimension of soot particles from premixed flames and motor vehicle exhaust, J. Aerosol Sci., 35, 1251–1274, doi:10.1016/j.jaerosci.2004.05.002, 2004.

McMeeking, G. R., Good, N., Petters, M. D., McFiggans, G., and Coe, H.: Influences on the fraction of hydrophobic and hydrophilic black carbon in the atmosphere, Atmos. Chem. Phys., 11, 5099–5112, doi:10.5194/acp-11-5099-2011, 2011.

Moteki, N. and Kondo, Y.: Effects of mixing state on black carbon measurements by laser-induced incandescence, Aerosol Sci. Technol., 41, doi:10.1080/02786820701199728, 398–417, 2007.

Ning, Z., Chan, K. L., Wong, K. C., Westerdahl, D., Močnik, G., Zhou, J. H., Cheung, C. S.: Black carbon mass size distributions of diesel exhaust and urban aerosols measured using differential mobility analyzer in tandem with Aethalometer, Atmos. Environ., 80, 31–40, doi:10.1016/j.atmosenv.2013.07.037, 2013.

Olfert, J. S., Symonds, J. P. R., and Collings, N.: The effective density and fractal dimension of particles emitted from a light-duty diesel vehicle with a diesel oxidation catalyst, J. Aerosol Sci., 38, 69–82, doi:10.1016/j.jaerosci.2006.10.002, 2007.

Pagels, J., Khalizov, A. F., McMurry, P. H., and Zhang, R. Y.: Processing of soot by controlled sulphuric acid and water condensation—mass and mobility relationship, Aerosol Sci. Technol., 43, 629–640, doi:10.1080/02786820902810685, 2009.

Park, K., Cao, F., Kittelson, D. B., and McMurry, P. H.: Relationship between particle mass and mobility for diesel exhaust particles, Environ. Sci. Technol., 37, 577–583, doi:10.1021/es025960v, 2003.

Park, K., Kittelson, D. B., and McMurry, P. H.: Structural properties of diesel exhaust particles measured by transmission electron microscopy (TEM): relationships to particle mass and mobility, Aerosol Sci. Technol., 38, 881–889, doi:10.1080/027868290505189, 2004.

Park, K., Dutcher, D., Emery, M., Pagels, J., Sakurai, H., Scheckman, J., Qian, S., Stolzenburg, M. R., Wang, X., Yang, J., and McMurry, P. H.: Tandem measurements of aerosol properties—a review of mobility techniques with extensions, Aerosol Sci. Technol., 42, 801–816, doi:10.1080/02786820802339561, 2008.

Peng, J. F., Hu, M., Guo, S., Du, Z. F., Zheng, J., Shang, D. J., Zamora, M. L., Zeng, L. M., Shao, M., Wu, Y.-S., Zheng, J., Wang, Y., Glen, C. R., Collins, D. R., Molina, M. J., and Zhang, R. Y.: Markedly enhanced absorption and direct radiative forcing of black carbon under polluted urban environments, Proc. Natl. Acad. Sci. USA, 113, 4266–4271, doi:10.1073/pnas.1602310113, 2016.

Raatikainen, T., Brus, D., Hooda, R. K., Hyvärinen, A.-P., Asmi, E., Sharma, V. P., Arola, A., and Lihavainen, H.: Size-selected black carbon mass distributions and mixing state in polluted and clean environments of northern India, Atmos. Chem. Phys., 17, 371–383, doi:10.5194/acp-17-371-2017, 2017.

Rissler, J., Nordin, E. Z., Eriksson, A. C., Nilsson, P. T., Frosch, M., Sporre, M. K., Wierzbicka, A., Svenningsson, B., Löndahl, J., Messing, M. E., Sjogren, S., Hemmingsen, J. G., Loft, S., Pagels, J. H., and Swietlicki, E.:

748   Effective density and mixing state of aerosol particles in a near-traffic urban environment, Environ. Sci.
749   Technol., 48, 6300–6308, doi:10.1021/es5000353, 2014.

750   Seinfeld, J. H., and Pandis, S. N.: Atmospheric chemistry and physics, Chapter 9–Dynamics of single aerosol
751   particles, John Wiley & Sons, Inc., Hoboken, New Jersey, 2006.

752   Scarnato, B. V., Vahidinia, S., Richard, D. T., Kirchstetter, T. W.: Effects of internal mixing and aggregate
753   morphology on optical properties of black carbon using a discrete dipole approximation model, Atmos. Chem.
754   Phys., 13, 5089−5101, doi:10.5194/acp-13-5089-2013, 2013.

755   Schwarz, J. P., Gao, R. S., Fahey, D. W., Thomson, D. S., Watts, L. A., Wilson, J. C., Reeves, J. M., Darbeheshti,
756   M., Baumgardner, D. G., Kok, G. L., Chung, S. H., Schulz, M., Hendricks, J., Lauer, A., Kärcher, B., Slowik,
757   J. G., Rosenlof, K. H., Thompson, T. L., Langford, A. Q., Loewenstein, M., and Aikin, K. C.: Single-particle
758   measurements of midlatitude black carbon and light-scattering aerosols from the boundary layer to the lower
759   stratosphere, J. Geophys. Res., 111, D16207, doi:10.1029/2006JD007076, 2006.

760   Schwarz, J. P., Gao, R. S., Spackman, J. R., Watts, L. A., Thomson, D. S., Fahey, D. W., Ryerson, T. B., Peischl, J.,
761   Holloway, J. S., Trainer, M., Frost, G. J., Baynard, T., Lack, D. A., de Gouw, J. A., Warneke, C., and Del Negro,
762   L. A.: Measurement of the mixing state, mass, and optical size of individual black carbon particles in urban and
763   biomass burning emissions, Geophys. Res. Lett., 35, L13810, doi:10.1029/2008GL033968, 2008.

764   Shiraiwa, M., Kondo, Y., Iwamoto, T., and Kita, K.: Amplification of light absorption of black carbon by organic
765   coating, Aerosol Sci. Technol., 44, 46–54, doi:10.1080/02786820903357686, 2010.

766   Slowik, J. G., Cross, E. S., Han, J. H., Kolucki, J., Davidovits, P., Williams, L. R., Onasch, T. B., Jayne, J. T., Kolb,
767   C. E., and Worsnop, D. R.: Measurements of morphology changes of fractal soot particles using coating and
768   denuding experiments: implications for optical absorption and atmospheric lifetime, Aerosol Sci. Technol., 41,
769   734–750, doi:10.1080/02786820701432632, 2007.

770   Sorensen, C. M.: The mobility of fractal agregates: A review, Aerosol Sci. Technol., 45, 765–779,
771   doi:10.1080/02786826.2011.560909, 2011.

772   Taylor, J. W., Allan, J. D., Liu, D., Flynn, M., Weber, R., Zhang, X., Lefer, B. L., Grossberg, N., Flynn, J., and Coe,
773   H.: Assessment of the sensitivity of core/shell parameters derived using the single particle soot photometer to
774   density and refractive index, Atmos. Meas. Tech., 8, 1701–1718, doi:10.5194/amt-8-1701-2015, 2015.

775   Wang, Q. Y., Huang, R. J., Cao, J. J., Han, Y. M., Wang, G. H., Li, G. H., Wang, Y. C., Dai, W. T., Zhang, R. J., and
776   Zhou, Y. Q.: Mixing state of black carbon aerosol in a heavily polluted urban area of China: implications for
777   light absorption enhancement, Aerosol Sci. Technol., 48, 689–697, doi:10.1080/02786826.2014.917758, 2014.

778   Wang, Y. Y., Liu, F. S., He, C. L., Bi, L., Cheng, T. H., Wang, Z. L., Zhang, H., Zhang, X. Y., Shi, Z. B., and Li, W.
779   J.: Fractal dimensions and mixing structrures of soot particles during atmospheric processing, Environ. Sci.
780   Technol. Lett., 4, 487–493, doi:10.1021/acs.estlett.7b00418, 2017.

781   Wu, Y. F., Zhang, R. J., Tian, P., Tao, J., Hsu, S.-C., Yan, P., Wang, Q. Y., Cao, J. J., Zhang, X. L., and Xia, X. A.:
782   Effect of ambient humidity on the light absorption amplification of black carbon in Beijing during January 2013,
783   Atmos. Environ., 124, 217–223, doi:10.1016/j.atmosenv.2015.04.041, 2016.

784   Wu, Y. F., Wang, X. J., Tao, J., Huang, R. J., Tian, P., Cao, J. J., Zhang, L. M., Ho, K.-F., Han, Z. W., and Zhang, R.
785   J.: Size distribution and source of black carbon aerosol in urban Beijing during winter haze episodes, Atmos.
786   Chem. Phys., 17, 7965–7975, doi:10.5194/acp-17-7965-2017, 2017.

787   Zhang, R. J., Jing, J., Tao, J., Hsu, S.-C., Wang, G., Cao, J., Lee, C.-S.-L., Zhu, L., Chen, Z., Zhao, Y. and Shen, Z.:
788   Chemical characterization and source apportionment of PM2.5 in Beijing: Seasonal perspective. Atmos. Chem.
789   Phys. 13, 7053–7074, doi:10.5194/acp-13-7053-2013, 2013.

790   Zhang, R. Y., Khalizov, A. F., Pagels, J., Zhang, D., Xue, H., Chen, J., and McMurry, P. H.: Variability in morphology,
791   hygroscopic and optical properties of soot aerosols during internal mixing in the atmosphere, Proc. Natl. Acad.

792   Sci. USA, 105, 10291–10296, doi:10.1073/pnas.0804860105, 2008.

793 Zhang, Y. X., Zhang, Q., Cheng, Y. F., Su, H., Kecorius, S., Wang, Z. B., Wu, Z. J., Hu, M., Zhu, T., Wiedensohler,

794   A., and He, K. B.: Measuring the morphology and density of internally mixed black carbon with SP2 and

795   VTDMA: new insight into the absorption enhancement of black carbon in the atmosphere, Atmos. Meas. Tech.,

796   9, 1833–1843, doi:10.5194/amt-9-1833-2016, 2016.